International Journal of Theoretical and Applied Research (IJTAR)

ISSN: 2812-5878

Homepage: https://ijtar.journals.ekb.eg

Original article

Investigation of Structural and Photoluminescence Properties of Neodymium-Doped Vanadium Pentoxide Thin Films Synthesized via Sol-Gel Route

Sh. Q. Seif[1], A. S. Abdel Moghny[2,*], Sh. n. Radwan[2] and A. A. Bahgat[2]

[1]MSc student, Department of Physics, Faculty of Science, Al-Azhar University., Nasr City, 11884 Cairo, Egypt.
[2] Department of Physics, Faculty of Science, Al-Azhar University., Nasr City, 11884 Cairo, Egypt.

ARTICLE INFO

Received 16/02/2025

Revised 03/05/2025

Accepted 03/05/2025

Keywords

$Nd_xV_2O_5.nH_2O$

Sol Gel

Raman spectroscopy

Photoluminescence (PL)

ABSTRACT

In this study, various compositions of $Nd_xV_2O_5.nH_2O$ with "x" ranging from 0 to 0.6 mol% were prepared. These nanocrystalline layers were synthesized via the sol-gel route. We investigated the intercalation effect of Nd+3 ions on the microstructure, vibrational, and optical behavior of $V_2O_5.nH_2O$ thin films using high-resolution X-ray diffraction (XRD), Fourier-transform infrared (FTIR) spectroscopy, Raman spectroscopy, and photoluminescence (PL) spectroscopy. XRD analysis revealed an orthorhombic structure with a preferred (001) orientation. Increasing neodymium content resulted in a decrease in crystallite size from 8.06 nm to 4.21 nm, with a corresponding increase in interlayer spacing from 1.09 nm to 1.32 nm, indicating successful intercalation of Nd+3 ions. FTIR spectroscopy verified the incorporation of Nd^{+3} ions by detecting shifts in the V=O stretching mode and the appearance of new peaks. Raman spectra analysis illustrated significant variations in the vibrational modes, including peak shifts, intensity variations, and the appearance of new peaks, specifically at higher Nd concentrations. Room temperature PL spectra analysis displayed three main emission peaks around 338 nm, 532 nm, and 720 nm, ascribed to defect states and band edge transitions in $V_2O_5.nH_2O$.

Graphical abstract

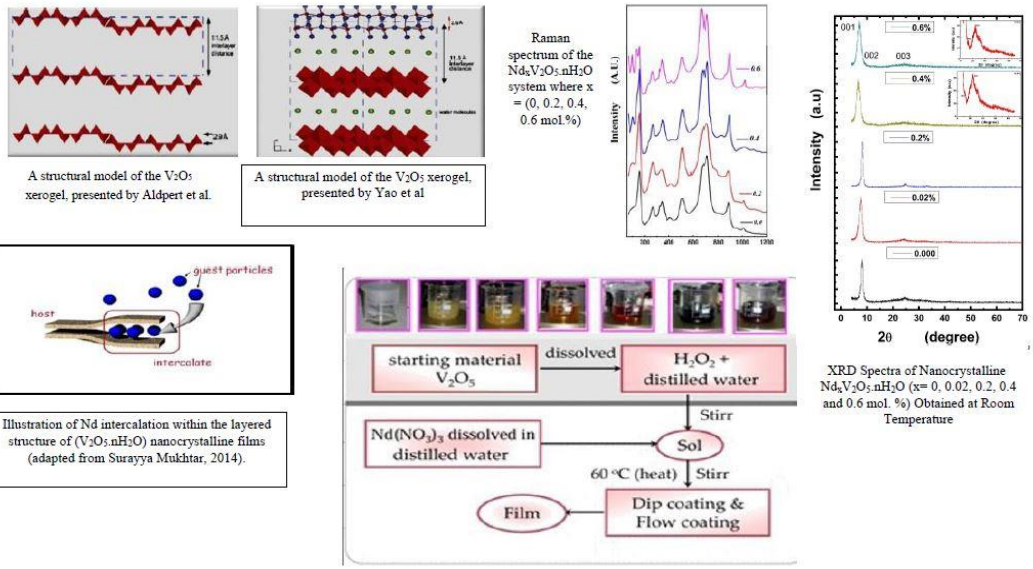

⁎ *Corresponding author*
E-mail address: abeersaid.519@azhar.edu.eg

DOI: **10.21608/IJTAR.2025.360956.1115**

1. Introduction

The driving force behind the research on the intercalation of rare earth elements (REE) in vanadium pentoxide xerogel ($V_2O_5.nH_2O$) is to investigate the effects of REEs on the crystalline structure and optical characteristics of $V_2O_5.nH_2O$. In modern daily life, optically transparent electronics are an essential part of modern technology. Recently, vanadium pentoxide (V_2O_5) thin-layer films have gained worldwide considerable interest because of their useful charge-carrying, catalytic and electrochemical attributes and behavior. Since 2011, continuous reports have highlighted the potential of 2D sheet material V_2O_5 for use in visible light applications without modifications [1].

Vanadium pentoxide is a semiconductor known for its high oxidizing properties, long-term chemical stability, and low toxicity, making it a preferred material for excellent photocatalysts [2]. Its unique optical characteristics enable it to absorb and reflect light within specific spectral bands, making it useful for optical devices and sensors. Its unique optical characteristics enable it to absorb and reflect light within specific spectral bands, making it useful for optical devices and sensors. The characteristics of vanadium pentoxide optical fibers have been widely studied [3]. In the field of material science, vanadium oxide compounds have gained significant attention because of their ability to tailor material characteristics based on oxidation states (V^{2+}, V^{3+}, V^{4+} and $^{V5+}$), with V_2O_5 being the most stable compound [4, 5].

Aldebert (1983) described the remarkable structure of vanadium pentoxide sol–gel, $V_2O_5.nH_2O$, as a host material with a layered structure composed of fibers and ribbons, with water molecules intercalating between its layers [6]. T. Yao and Y. Oka in 1997 showed that vanadium pentoxide, V_2O_5, exhibits a lamellar structure (see Figs. 1 and 2) [7]. Its deformed orthorhombic structure, resembling a flat sheet, is considered the key determinant of its distinctive optical behavior. It also offers a promising starting point for various combinations produced by doping elements, which fundamentally alter the structural and optical properties [8]. V_2O_5 xerogel exhibits a layered structure similar to clay, but with weaker interlayer electrostatic forces due to the presence of dissociable H_2O molecules and cations, making it more flexible for intercalation [9].

Doping V_2O_5 with additional elements can modify the material's electronic structure and band gap, thereby exerting an influence on its optical properties [10]. REEs are among the most interesting elements that intercalate into V_2O_5 xerogel because of their strong 4f intra-shell emission [11]. Rare-earth elements (lanthanides), and their doped materials are vital for modern technology, valuable for up-conversion, solar energy, lasers, optical amplifiers, and smart sensors [12, 13].

Neodymium (Nd), a prominent Rare Earth Element (REE) and the third most abundant lanthanide following cerium and lanthanum, exhibits an electronic structure characterized by the [Xe] $4f^4 6s^2$ electron configuration and possesses an atomic radius of 181 pm [14]. Applications of neodymium include the production of high-strength magnets and laser crystals like Nd:YAG. [15].

Neodymium metal, along with iron and boron, forms very powerful permanent magnets that are cheaper, lighter and stronger making them widely used in electronic gadgets [16]. A series of Nd-doped V_2O_5 thin films with varying compositions were synthesized to study the influence of Nd^{3+} ions on the nano-structural and optical behavior of $V_2O_5.nH_2O$ [14]. The physical properties of a material, such as refractive index, extinction coefficient, homogeneity, density, hardness, internal stress, and crystal structure, are significantly affected by the chosen preparation and deposition methods [17]. Techniques like pulsed laser deposition, vacuum evaporation, solid-state synthesis, and gas-phase methods each offer distinct advantages, allowing for tailored properties to meet specific application requirements [18].

A novel sol–gel-based material synthesis is introduced in this research with the aim of achieving high crystallinity, reduces particle size, and controls product dimensionality without post-thermal treatment. This method significantly reduces impurities and enhances homogeneity, producing uniformly sized nanometer-sized particles [19]. It is suitable for preparing thin films for optical property analysis. Figure 3 illustrates how neodymium nitride, after dissolving in distilled water, intercalates into the vanadium pentoxide layers through the sol–gel process.

In the current research, we focus on the intercalation of neodymium nitride into the V_2O_5 layers during the sol–gel process. We aim to study the effects of neodymium on structural and photoluminescence properties of vanadium pentoxide xerogel, with potential for significant technological applications.

2. Materials and Methods

2.1 Raw Materials

- Neodymium (III) nitrate [Nd $(NO_3)_3$], crystalline, highly water-soluble (suitable for low pH applications 99.9%)
- Vanadium pentoxide (V_2O_5), 99.9% purity
- Hydrogen peroxide (H_2O_2), 17.5% solution
- Distilled water
- Pyrex substrates

2.2 Synthesis of $Nd_xV_2O_5{\cdot}nH_2O$ Thin Films

- **$V_2O_5.nH_2O$ Preparation:**

At room temperature, 1.04 g of V_2O_5 was added to a mixture of 60 mL of 17.5% hydrogen peroxide and 20 mL of distilled water. After one hour of magnetic stirring, the solution was heated to 60°C while maintaining constant stirring and a pH range of 3–4, resulting in a brown suspension.

- **Neodymium Incorporation:**

To ensure precise Nd doping, the required amount of $[Nd(NO_3)_3]$ was dissolved in 20 mL of distilled water

and gradually added to the V_2O_5 gel with a burette, adjusting the concentration (x) as needed.

Chemical Reactions:
These equations represent the reactions that occur during the synthesis process:
$Nd(NO_3)_3(s) \rightarrow Nd^{3+}(aq) + 3NO_3^-(aq)$
$V_2O_5 \cdot nH_2O + xNd^{3+} \rightarrow NdxV_2O_5 \cdot nH_2O$

2.3 Film Deposition
The resulting sol gel was deposited onto Pyrex substrates using either dip and flow-coating techniques. Subsequent to deposition, the films were air-dried spontaneously to achieve the desired orientation of the layered plane.

2.4 Characterization
The synthesized films were characterized using various techniques:

- A PANalytical X'Pert Pro MRD X-ray diffractometer, equipped with a CuKα radiation source (λ = 1.5406 Å), was used to obtain XRD spectra. Data collection was conducted in the 2θ range of 4°–90° with a step increment of 0.02°.
- The film thicknesses (d) were measured using an optical interference technique with a ZYGO-Maxim Interferometer microscope, and the results are presented in Table 1.
- The FT/IR Spectrometer (Nicolet iS50) was employed to measure the infrared spectra in the range of 400-4000 cm^{-1}, providing insight into the vibrational characteristics of the functional groups in the samples.
- Using the Xplora Plus Raman microscope and a 10x magnification objective, Raman scattering studies were conducted at room temperature in air, employing a 532 nm wavelength for excitation.
- A Spectrofluorophotometer RF-5301PC, equipped with a 150 W Xenon lamp and a 240 nm wavelength, was used for room temperature PL measurements on all samples.

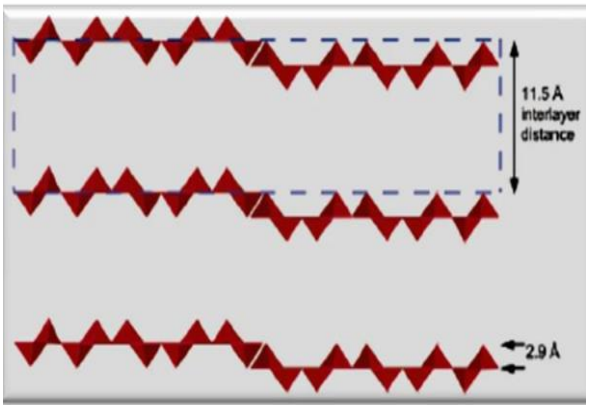

Fig.1 A structural model of the V_2O_5 xerogel, presented by Aldpert et al. [5].

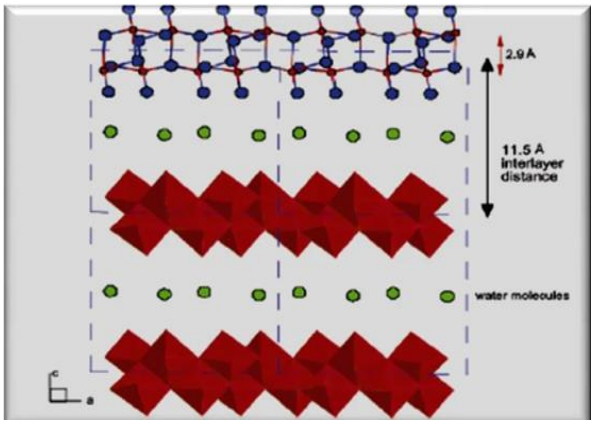

Fig.2 A structural model of the V_2O_5 xerogel, presented by Yao et al. [7].

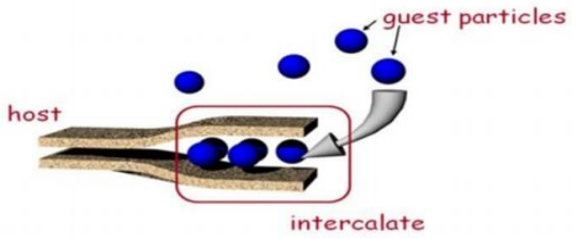

Fig.3 Illustration of Nd intercalation within the layered structure of ($V_2O_5.nH_2O$) nanocrystalline films (adapted from Surayya Mukhtar, 2014).

3. Experimental Results and Analysis
3.1 X-ray Diffraction Analysis of Thin Films
XRD measurements were performed to investigate the crystal structure and size of crystallites in $Nd_xV_2O_5.nH_2O$ thin films (where x = 0, 0.02, 0.2, 0.4 and 0.6 mol. %) prepared by the sol-gel procedure under room temperature (Fig. 4). XRD analysis of the prepared samples revealed a crystalline nature with prominent peaks at (001), (003), (004), and (005), confirming a well-defined preferred orientation. The obtained results show excellent agreement with the standard JCPDS data (card no: 40-1296), with no remarkable peaks of impurity phases detected. This indicates that the structure of the host material remains unaffected, with no secondary phases as Nd or Nd_2O_3 were detected. The un-doped sample exhibited a strong c-axis orientation, with the most intense XRD peak at 2θ = 8.07° (d spacing = 1.09 nm) corresponding to the (001) plane. This confirms that vanadium pentoxide xerogel ribbons are stacked in a one-dimensional manner, oriented perpendicular to the substrate, with vanadium-oxygen layers consisting of interconnected fibers and water molecules.

The observed shift in the Bragg angle to lower values (approximately 1°) with increasing Nd^{3+} content can be ascribed to the lattice strain generated by the disparity in ionic radii between the Nd^{3+} and V^{5+} ions. The intercalation of Nd^{3+} ions is evidenced by a slight increase in the interlayer spacing (d_{001}) as shown in Fig. 5 [20, 21]. The observed XRD data, including peak shifts and changes in interlayer spacing, may be indicative of a structural rearrangement where a loss of intercalated water results in increased attractive interactions between the positively charged ions and the negatively charged V_2O_5 layers,

possibly due to enhanced polarization forces [22]. At higher dopant concentrations (0.4 and 0.6 mol. %), a small peak (002) reflection at 2θ =12.05° was detected, corresponding to neodymium oxide (Nd_2O_3), indicating the incorporation of Nd^{3+} ions into the V_2O_5 lattice. The data suggests that as Nd concentration increases, the diffraction peak area of the (002) planes also slightly increases, indicating Nd^{3+} ion intercalation within the interlayer, while a decrease in water content or adsorbed water is observed [23].

Increasing Nd^{3+} content causes diffraction peak broadening, reflecting reduced crystallite size as shown in table 1, which aligns with Debye-Scherrer's equation [24, 25]:

$$D = k\lambda / (\beta \cos \theta) \quad (1)$$

Internal stress increases, leading to lattice distortion and consequently inhibiting the growth of V_2O_5 crystallites [26].

Figure 6 presents a W-H plot, a graphical tool used to distinguish between crystallite size and strain effects on peak broadening in the XRD profiles of $Nd_xV_2O_5.nH_2O$ thin films.

In the W-H plot, the average crystalline size and the strain created throughout the preparation procedures are calculated using the formula:

$$\beta \cos\theta = \lambda c / D + 2 \epsilon \sin\theta \quad (2)$$

with c, the correction factor, is assumed to be unity, and ϵ denoting the strain. [27]. The origin of strain is related to lattice "misfit" and to the film/substrate interface as well which in turn depends upon the growing condition of the film [24]. The estimation of micro-strain within the films is achieved by analyzing the slope of the linear curve in Fig. 6, as dictated by the relationship outlined in Eq. 2. Thin film dislocation density (δ) is given by [28]:

$$\delta = n/D^2 \quad (3)$$

with n taken as 1. The obtained results are summarized in Table 1 and presented in Fig. 5. Scherrer equation is based on a Gaussian distribution of crystallite sizes, whereas the Williamson-Hall Plot method accounts for strain factors that can influence peak broadening in diffraction spectra, resulting in varied crystallite size calculations.

3.2 FT-IR Spectroscopic Investigation

FTIR spectroscopy is instrumental in detecting functional groups and chemical bonds by studying molecular vibrations within the $Nd_xV_2O_5.nH_2O$ system. FTIR transmittance spectra of V_2O_5 xerogels, as reported in recent literature, display characteristic absorption bands due to V=O and V–O vibrations and intercalated water.

FTIR spectra of $Nd_xV_2O_5.nH_2O$ thin films (where $0 \leq x \leq 0.6$ mol. %) synthesized by the sol gel procedure under normal conditions are depicted in Fig. 7. The $Nd_xV_2O_5.nH_2O$ system exhibited a series of vibrational

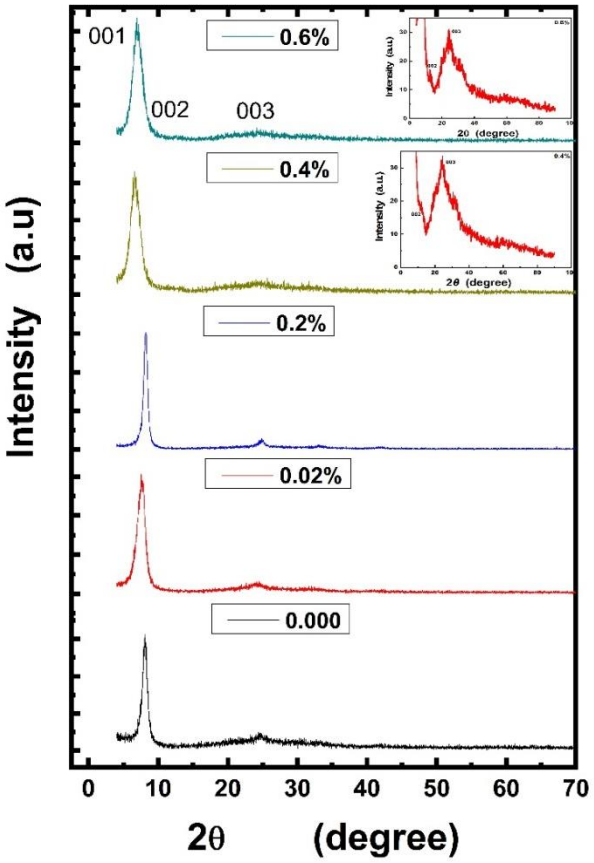

Fig. 4: XRD Spectra of Nanocrystalline $Nd_xV_2O_5.nH_2O$ (x= 0, 0.02, 0.2, 0.4 and 0.6 mol. %) Obtained at Room Temperature.

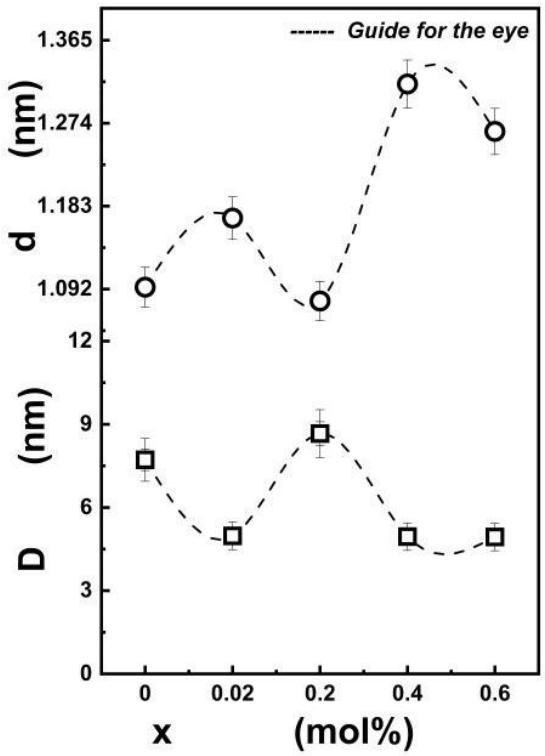

Fig.5: Lattice constant (d_{001}) and crystallite size (D) derived from XRD analysis of sol-gel- synthesized $Nd_xV_2O_5{\cdot}nH_2O$ nanostructures.

bands at 520, 682, 763, 917, 1006, 1404, 1616, 2927.9, 2958, and 3398 cm^{-1}. The 520 cm^{-1} band is characteristic of edge-sharing V-O stretching, while the 764 cm^{-1} and 918 cm^{-1} bands likely correspond to VO_4 tetrahedral and VO_5 pyramid bond stretching, respectively [29]. The band at 1006 cm^{-1} is assigned to the V=O stretching vibration of the vanadyl group [30].

The 1006 cm^{-1} peak in Nd-doped V_2O_5 spectra is observed to shift towards higher wavenumbers compared to pure V_2O_5, indicating the incorporation of Nd^{3+} ions within the lattice, their proximity to oxygen atoms, and a distortion of the V=O bond [31]. Furthermore, a shift of the 682 cm^{-1} band towards lower wavenumbers is observed, which may be associated with a change in the valence state of vanadium from V^{5+} to V^{4+} [21]. New peaks at 1830 cm^{-1} and 2367 cm^{-1} observed in Nd-doped V_2O_5 spectra indicate altered V=O stretching. This suggests Nd ion intercalation, modifying the force constant and influencing O-H (hydroxyl group) vibrational modes [32].

3.3 Raman Spectra Analysis

Raman spectroscopy is an effective tool for explaining the effects of structural order and disorder in the $Nd_xV_2O_5.nH_2O$ system. Raman spectra of $Nd_xV_2O_5.nH_2O$, where x = (0, 0.2, 0.4, 0.6 mol. %), are depicted in Fig. 8. For all samples, Raman band detected around 155 cm^{-1} aligns with those documented in the literature at approximately 148 cm^{-1} for crystalline V_2O_5 [33]. The shifting observed from 148 cm^{-1} in crystalline to 155 cm^{-1} in V_2O_5 gel confirms that all prepared samples are a perfect gel with a less crystalline structure. Raman spectrum of pure V_2O_5 exhibits several characteristic peaks that provide insights into the structural features of the material. The main Raman peak at low-frequency located at approximately 155 cm^{-1}, a fingerprint of $[VO_5]$-$[VO_5]$ vibrations (literature: ~148 cm^{-1}) arising from lattice-bending, providing strong evidence for the well-ordered layered structure of V_2O_5.

The peak at 266 cm^{-1} is attributed to V=O (terminal oxygen) bending vibrations [1]. The Peaks positioned at ~325, and 403 cm^{-1} are attributed to $V_3{-}O_C$ (triply coordinated oxygen) and $V{-}O_B{-}V$ bending vibrations, respectively. Furthermore, the peak around 706 cm^{-1} is associated with $V_2{-}O_B$ (doubly coordinated oxygen) stretching, characteristic of corner-sharing oxygen atoms between two pyramids. The high-frequency Raman peak observed at approximately 1005 cm^{-1} is characteristic of the stretching vibration of the vanadyl oxygen (V=O) bond, as reported in the literature [34]. Finally, the band at 947 cm^{-1}, aligning with literature values (934 cm^{-1}) for amorphous V_2O_5, is typically associated with V^{4+}=O bonds [35].

Raman spectra of Nd-doped $V_2O_5.nH_2O$ samples show slight variations compared to pure V_2O_5. These variations are indicated by shifts in peak positions, alterations in peak intensities, splitting of the peaks, and the appearance of new peaks. The low - frequency vibration band observed at 155 cm^{-1} for pure V_2O_5 and low concentration Nd-doped samples (0, 0.2% and 0.4%) appears to be narrow and sharp, suggesting a three-dimensional and along range order for low concentration of Nd ions in the prepared samples. In contrast, with increasing doing ratio up to 0.6% of Nd^{3+}3 ions a splitting of bands is observed in the rage (120 - 160 cm^{-1}) and (650 – 710 cm^{-1}), which may be attributed to lattice distortion and strain caused by the doping of Nd^{+3} ions with ionic radius larger than V^{+5} between the layers of V_2O_5.

The size mismatch and variation of bonding properties of Nd^{+3} ions compared to V^{+5} ions may result in symmetry breaking of the V_2O_5 lattice, leading to splitting or multiple peaks observed in this wavenumber region [36].

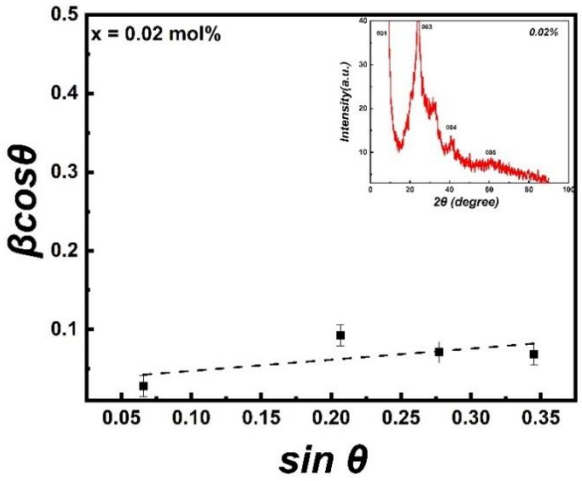

Fig. 6: Graphical representation of size-strain behavior following Eq. (2).

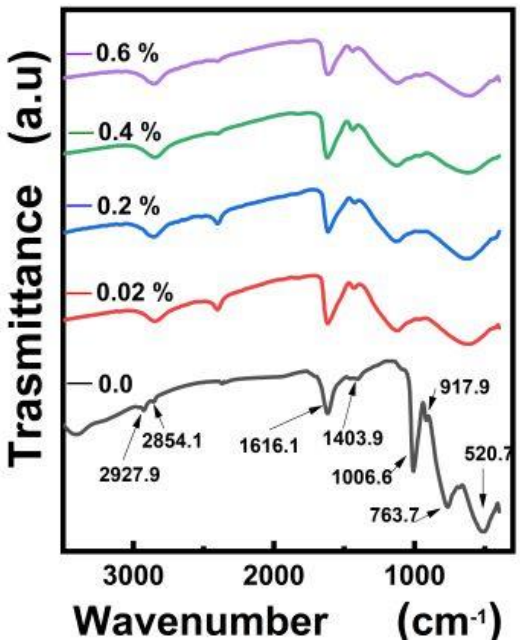

Fig.7: FTIR spectra of $Nd_xV_2O_5.nH_2O$ thin films showing transmittance trends as a function of Nd concentration (x= (0, 0.02, 0.2, 0.4, 0.6 mol. %).

Table 1: A Comprehensive Overview of X-ray Structural Data for $Nd_xV_2O_5.nH_2O$ Thin Films, including Interlayer Spacing (d_{001}), Particle Size (D), Micro-strain (ε), and Dislocation Density (δ).

x (mol%)	D (nm) Scher.equ.	D (nm) W-H method	d_{001} (nm)	δ ($nm^2 \times 10^{-2}$)	ϵ	d (nm)
0	8.06	5.87	1.09	3.13	0.063	285
0.02	4.98	4.35	1.17	4.06	0.141	469
0.2	8.66	9.87	1.08	1.33	0.063	355
0.4	4.21	3.46	1.32	5.18	0.194	269
0.6	4.39	2.78	1.26	4.63	0.129	284

Additionally, new peaks are observed with a high concentration of Nd-doped samples (such as 0.6% Nd ions) at around 98 cm^{-1},130 cm^{-1}, 226 cm^{-1}, 303 cm^{-1} and 667 cm^{-1}. the appearance of new peaks for Nd-doped V_2O_5 in the Raman spectra, particularly at high concentrations, may be related to a new Raman-active modes induced by Nd^{3+} ions that are introduced between V_2O_5 layers and change the local symmetry of the V_2O_5 lattice, resulting in new modes that can be recorded as new peaks in the Raman spectrum.

The combination of FTIR and Raman analyses reveals compelling evidence that Nd^{3+} doping induces significant structural modifications in V_2O_5, including lattice distortions and the formation of mixed valence oxide species (VO_4), resulting in a lower work function and reduced electron-hole recombination, leading to improved photocatalytic efficiency in methylene blue dye degradation [32]. Furthermore, alterations in Raman peak intensities for Nd-doped samples are observed in the Raman Spectrum. This alterations in intensities may result from modifications in the polarizability of the vanadium-oxygen bonds or changes in the long-range and short-range ordering of the V_2O_5 lattice structure caused by the doping of Nd^{+3} ions. Similar effects observed with Mn, Ni, and Fe on the layered structure of the V_2O_5 lattice [32, 37, 38] support this conclusion. The significant effects of Nd^{+3} doping on Raman spectra, including shifts in Raman modes and crystal lattice disorder, are similar to the results observed with Nd^{+3} doping on uranium dioxide reported by Lee et al. (2024), which studied how the incorporation of neodymium (Nd^{3+}) ions impacts the crystalline structure and electrochemical responses of uranium dioxide (UO_2), a material with vital role in nuclear applications [39].

XRD, FTIR, and Raman analyses collectively indicate that Nd^{3+} doping induces structural and chemical changes in the V_2O_5 lattice. XRD displays new diffraction peaks and changes in Bragg angles, indicating secondary phases and Nd^{3+} intercalation. In accordance with the structural changes observed in XRD, FTIR confirms novel absorption bands and shifts in V=O stretching modes. Raman spectra display shifts and new peaks, resulting in changes in vibrational modes and crystallinity, confirming dopant-induced changes that aligns with XRD and FTIR results.

3.4 Photoluminescence Response and Interpretation

The room temperature photoluminescence (PL) spectra of pure V_2O_5 and $Nd_x.V_2O_5.nH_2O$ thin films (where x = 0, 0.4, 0.6 mol.%) are displayed in Fig.18, using an excitation wavelength of 240 nm. A highly intense emission peak observed around 480 nm for all samples may be attributed to the glass substrate used for the deposition of thin films.

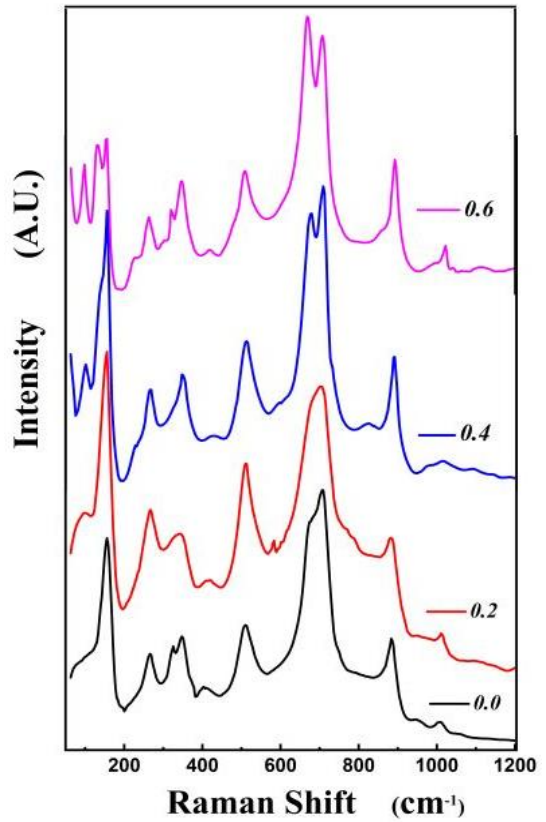

Fig.8 Raman spectrum of the $Nd_xV_2O_5.nH_2O$ system where x = (0, 0.2, 0.4, 0.6 mol.%)

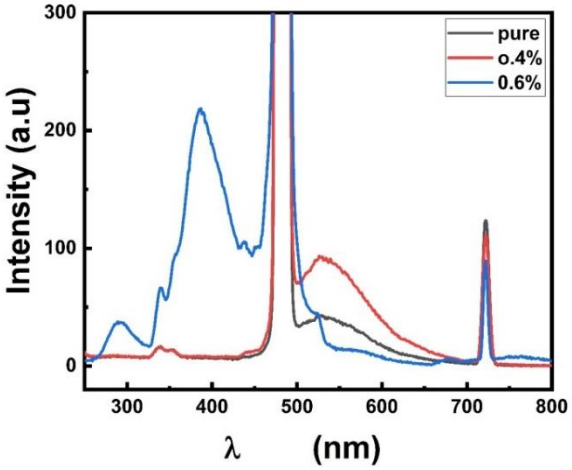

Fig.9: Room-temperature PL spectra of Nd-doped V_2O_5 for different Nd concentrations.

The obtained PL spectra reveal three main peaks recorded for all samples, differing in intensity with varying ratios of Nd^{+3} ions. The (PL) peak observed at around 532 nm (corresponding to 2.34 eV) is ascribed to the band-edge transition in V_2O_5, associated to the band gap energy of V_2O_5, which falls within the range of 2.3 to 2.4 (eV) [32,38,40]. The PL spectra (Figure 9) show defect-related emissions at 338 nm (attributed to V^{4+} centers) [40] and 720 nm (oxygen defects) [32], which are known to enhance photocatalytic activity by providing active sites for redox reactions, as observed in similar V_2O_5based systems [2, 11]. According to these studies, the resulting UV emission may be attributed to electron-hole recombination at these sites, indicating the presence of V^{4+} centres (Vanadium in a lower oxidation state) as reported in [40]. The photoluminescence (PL) spectra of the undoped V_2O_5 samples are significantly influenced by the doping of Nd^{+3} ions, as evidenced by changes in the intensity of emission peaks and the appearance of a new peaks. The photoluminescence (PL) spectra of the undoped V_2O_5 samples are significantly influenced by the doping of Nd^{+3} ions, as evidenced by changes in the intensity of emission peaks and the appearance of a new peaks.

For the high concentration of Nd-doped V_2O_5 (0.6% mol.), additional emission peaks are observed cantered around 290 nm and 679 nm. These new peaks may be related to intra-4f transitions of Nd^{3+} ions. The origin of the visible emissions i.e. the red emissions has been associated with the recombination process of electrons in the shallow defect levels with the photo -excited holes in the valence band, arising from the $^4\mathbf{I}_{9/2} \rightarrow {}^2\mathbf{H}_{11/2}$ transition [31, 41].

4. Conclusion

Neodymium-doped vanadium pentoxide (Nd: $V_2O_5.nH_2O$) thin films were synthesized using the sol-gel method, yielding high-quality nanocrystalline layers with optimized properties. High-resolution X-ray diffraction (XRD) analysis confirmed the incorporation of Nd^{3+} ions, revealing an orthorhombic structure with a preferred (001) orientation. Doping reduced crystallite sizes from 8.06 nm to 4.21 nm and increased interlayer spacing from 1.09 nm to 1.32 nm. Fourier-transform infrared (FTIR) and Raman spectroscopy validated these changes, displaying shifts in vibrational modes and new peaks at higher Nd concentrations, indicating structural and chemical modifications. Optical analysis revealed two band gaps: an indirect forbidden transition (E_{Op1}, r = 1/3) ranging from 0.288 to 0.331 eV and a direct forbidden transition (E_{Op2}, r = 3/2) from 2.25 to 2.41 eV, suggesting multiple conduction mechanisms. Photoluminescence (PL) spectra exhibited emission peaks at 338 nm, 532 nm, and 720 nm due to defect states and band-edge transitions, with the 720 nm red emission linked to electron-hole recombination, and Nd^{3+}specific intra-4f emissions at 290 nm and 679 nm at higher doping levels. These properties enable applications in photocatalysis for methylene blue degradation in water purification, optoelectronics (photodetectors and LEDs), chromogenic smart windows, photonic devices (lasers and up-conversion phosphors), optical/chemical sensors, and energy storage (supercapacitors and batteries), offering significant potential for technological advancements.

Declarations

Competing interests: The authors confirm that no competing interests, financial or personal, influenced the conclusions of this research.

Data Availability:

The data supporting the conclusions of this work are available in the article.

References

1. Wang, S., Wu, L., Zhang, H., Wang, Z., Qin, Q., Wang, X., Lu, Y., Li, L., Li, M. Facile synthesis of two-dimensional (2D) V_2O_5 nanosheets film towards photodetectors. Materials, **15** (2022) 8313. https://doi.org/10.3390/ma15238313
2. Yu, Y., Ming, H., He, D., Li, J., Jin, Y., Sun, H., Ahmad, M., & Wang, X. V_2O_5-based photocatalysts for environmental improvement: Key challenges and advancements. Journal of Environmental Chemical Engineering, 11(6) (2023) 111243. https://doi.org/10.1016/j.jece.2023.111243
3. Dhawan, A., Sharma, Y., & Brickson, L. L. Incorporation of vanadium oxide films in optical fibers for temperature sensing and optical switching applications. Optical Materials Express, 4(8) (2014) 1128-1135. https://doi.org/10.1364/OME.4.001128
4. Hu, P., Hu, P., Vu, T. D., Li, M., Wang, S., Ke, Y., Zeng, X., Mai, L., & Long, Y. Vanadium oxide: Phase diagrams, structures, synthesis, and applications. Chemical Reviews, 123(8) (2023) 4353–4415. https://doi.org/10.1021/acs.chemrev.2c00546
5. Legendre, J., Aldebert, P., Baffier, N., & Livage, J. Vanadium pentoxide gels: II. Structural study by x-ray diffraction. Journal of Colloid and Interface Science, 94(1) (1983) 84-89. https://doi.org/10.1016/0021-9797(83)90237-0
6. Legendre, J., Aldebert, P., Baffier, N., & Livage, J. Vanadium pentoxide gels: II. Structural study by x-ray diffraction. Journal of Colloid and Interface Science, 94(1) (1983) 84-89. https://doi.org/10.1016/0021-9797(83)90237-0
7. Yao, T., Oka, Y., & Yamamoto, N. Layered structures of vanadium pentoxide gels. Materials Research Bulletin, 27(6) (1992) 669-675. https://doi.org/10.1016/0025-5408(92)90073-9
8. Yu, Z., Zheng, J., Jing, X., Hang, G., Liu, Q., & Cai, W. Study on the optical and electrochemical performance of V_2O_5 with various morphologies. Journal of Dispersion Science and Technology, 41(14) (2020). https://doi.org/10.1080/01932691.2019.1656085
9. Kristoffersen, H., & Metiu, H. Structure of $V_2O_5 \cdot nH_2O$ xerogels. The Journal of Physical

Chemistry C, 120(7) (2016) 4353–4415. https://doi.org/10.1021/ACS.JPCC.5B12418

10. Altowyan, A. S., Hakami, J., Algarni, H., & Shkir, M. Enhancing the optoelectronic properties of V_2O_5 thin films through Tb doping for photodetector applications. Journal of Alloys and Compounds, 960 (2023) 170911. https://doi.org/10.1016/j.jallcom.2023.170911.
11. Kabir, M. H., Hossain, M. Z., Jalil, M. A., Hossain, M. M., Ali, M. A., Khandaker, M. U., Jana, D., Rahman, M. M., Hossain, M. K., & Uddin, M. MEnhancement of photocatalytic performance of V_2O_5 by rare-earth ions doping, synthesized by facile hydrothermal technique. ArXiv: 2301.06666 . (2023) [physics.chem-ph]. https://doi.org/10.48550/arXiv.2301.06666
12. Yang, W., Li, X., Chi, D., Zhang, H., & Liu, X. Lanthanide-doped upconversion materials: emerging applications for photovoltaics and photocatalysis. Nanotechnology, 25(48) (2014) 482001. https://doi.org/10.1088/0957-4484/25/48/482001
13. Eliseeva, S. V., & Buenzli, J.-C. G. Rare earths: jewels for functional materials of the future. New Journal of Chemistry, 35 (2011) 1165-1176. https://doi.org/10.1039/c0nj00969e
14. Generalic, E. Neodymium. In EniG. Periodic Table of the Elements. KTF-Split. Retrieved September 5 (2024) 2024, from https://www.periodni.com/nd.html
15. Semwal, K., & Bhatt, S. C. Study of Nd^{3+} ion as a Dopant in YAG and Glass Laser. International Journal of Physics, 1(1) (2013) 15-21. https://doi.org/10.12691/ijp-1-1-3
16. Herbst, J. F., Lee, R. W., & Pinkerton, F. E. Rare Earth-Iron-Boron Materials: A New Era in Permanent Magnets. Annual Review of Materials Research, 16 (1986) 467-485. https://doi.org/10.1146/annurev.ms.16.080186.002343
17. Rondiya, S. R., Roy, A., Rahane, G. K., Jadhavar, A., Kamble, M. M., Puneeth, K. P., Hareesh, K., Suryawanshi, M. P., Dzade, N. Y., & Jadkar, S. R Physical Methods for Synthesis and Thin-Film Deposition. In Applications of Nanomaterials for Energy Storage Devices (1st ed., pp. 77-96) (2022). CRC Press. https://doi.org/10.1201/9781003216308-4
18. Ohring, M. Materials science of thin films: deposition and structure (2nd ed.). Academic Press. ISBN: 0125249756. (2002).
19. Hassen, A., El Sayed, A. M., Al-Ghamdi, A., & Shaban, M. Synthesis of Some Functional Oxides and Their Composites Using Sol-Gel Method. In Open Access Peer-Reviewed Chapter (2023). http://dx.doi.org/10.5772/intechopen.111384
20. Özdemir, O., Gökdemir, F. P., Menda, U. D., Kavak, P., Saatci, A. E., & Kutlu, K. Nano-Crystal $V_2O_5{\cdot}nH_2O$ Sol-Gel Films Made by Dip Coating. AIP Conference Proceedings, 1476 (2012) 233–240. https://doi.org/10.1063/1.4751601
21. Govindarajan, D., & Uma Shankar, V. Structural and Morphological Characterization of Nd Doped V_2O_5 Nanorods. International Journal of Innovative Technology and Exploring Engineering, 9(1) (2019) 2050. https://doi.org/10.35940/ijitee.L3856.119119
22. Özdemir, O., Gökdemir, F. P., Menda, U. D., Kavak, P., Saatci, A. E., & Kutlu, K. Influence of Water Expulsion on Structural Properties of $V_2O_5{\cdot}nH_2O$ Sol-Gel Films. In AIP Conference Proceedings, 1476(1) (2012) 279-284. https://doi.org/10.1063/1.4751611
23. Balasubramani, V., Chandrasekaran, J., Manikandan, V., Marnadu, R., Vivek, P., & Balraju, P. Influence of rare earth doping concentrations on the properties of spin coated V_2O_5 thin films and Cu/Nd-V_2O_5/n-Si Schottky barrier diodes. Inorganic Chemistry Communications, 119 (2020) 108072. https://doi.org/10.1016/j.inoche.2020.108072
24. Negm, S.E., Mady, H.A., Abdel Moghny, A.S., Abd-Rabo, A.S., & Bahgat, A.A. Structural properties of $K_xV_2O_5.nH_2O$ nanocrystalline films. Solid State Sciences, 13 (2011) 590–595. https://doi.org/10.1016/j.solidstatesciences.2010.12.031
25. Iida, Y., & Kanno, Y. Doping effect of M (M = Nb, Ce, Nd, Dy, Sm, Ag, and/or Na) on the growth of pulsed-laser deposited V_2O_5 thin films. Journal of Materials Processing Technology, 209(5) (2009) 2421-2427. https://doi.org/10.1016/j.jmatprotec.2008.05.033
26. Jassim, I. K., Rzaij, J. M., Ali, I. M., & Ibrahim, I. M. Influence of Nd and Ce doping on the structural, optical and electrical properties of V_2O_5 thin films. Iraqi Journal of Physics, 14(30) (2016) 73-82. https://doi.org/10.30723/ijp.v14i30.202
27. Rani, S., Bansal, K., Rani, N., Ilyas, M., Singh, G., & Singh, S. Facile solution combustion based synthesis of V_2O_5 nanocrystals and size-strain study by XRD analysis. In AIP Conference Proceedings, 2352(1) (2021) 040024. https://doi.org/10.1063/5.0052508
28. Amlouk, A., Boubaker, K., Amlouk, M., & Bouhafs, M. Study of ytterbium doping effects on structural, mechanical and opto-thermal properties of sprayed ZnO thin films using the Boubaker polynomials expansion scheme (BPES). Journal of Alloys and Compounds, 485(1–2) (2009) 887–891. https://doi.org/10.1016/j.jallcom.2009.05.029
29. Guerra, E. M., Silva, G. R., & Mulato, M. Extended Gate Field Effect Transistor Using V_2O_5 Xerogel Sensing Membrane by Sol-Gel Method. Solid State Sciences, 11(2) (2009) 456-460. http://dx.doi.org/10.1016/j.solidstatesciences.2008.07.014
30. Brázdová, V., Ganduglia-Pirovano, M. V., & Sauer, J. Vanadium oxides on aluminum oxide supports. 2. Structure, vibrational properties, and reducibility of V_2O_5 clusters on alpha-Al_2O_3 (0001). Journal of Physical Chemistry B, 109(22) (2005) 10909-10916. https://doi.org/10.1021/JP0539167

31. Venkatesan, A., Chandar, N. R. K., Kandasamy, A., Chinnu, M. K., Marimuthu, K. N., Kumar, R. M., & Velc, R. J. Luminescence and electrochemical properties of rare earth (Gd, Nd) doped V_2O_5 nanostructures synthesized by a non-aqueous sol–gel route. RSC Advances, 5(19) (2015) 14265-14274. http://dx.doi.org/10.1039/C4RA14542A
32. Le, T. K., Pham, P., Dong, C.-L., Bahlawane, N., Vernardou, D., Mjejri, I., Rougier, A., & Kim, S. W. Recent advances in vanadium pentoxide (V_2O_5) towards related applications in chromogenics and beyond: fundamentals, progress, and perspectives. Journal of Materials Chemistry C, 10(11) (2022) 4019-4071. https://doi.org/10.1039/D1TC04872D
33. Sanchez, C., & Livage, J. Infrared and Raman Study of Amorphous V_2O_5. Journal of Raman Spectroscopy, 12(1) (1982) 1-6. https://doi.org/10.1002/jrs.1250120102
34. Dhananjaya, M., Guru Prakash, N., Lakshmi Sandhya, G., Lakshmi Narayana, A., & Hussain, O.M. Microstructure and Supercapacitor Properties of V_2O_5 Thin Film Prepared by Thermal Evaporation Method. Mechanics, Materials Science & Engineering, 2(2017) 1-6. https://doi.org/10.2412/2412-5954.
35. Ureña-Begara, F., Crunteanu, A., & Jean-Pierre. Raman and XPS characterization of vanadium oxide thin films with temperature. Applied Surface Science, 403(2017) 717–727. https://doi.org/10.1016/j.apsusc.2017.02.067
36. Kim, Y. H., Kim, H. J., Ong, S. P., Wang, Z., & Im, W. B. Cation-Size Mismatch as a Design Principle for Enhancing the Efficiency of Garnet Phosphors. Chemistry of Materials, 32(7) (2020) 3097−3108. https://dx.doi.org/10.1021/acs.chemmater.0c00095
37. Yong, W., Zhang, H. L., Cao, H. T., Tian, T., Gao, J. H., Liang, L. Y., & Zhu, F. Effect of post-annealing on structural and electrochromic properties of Mo-doped V_2O_5 thin films. Journal of Sol-Gel Science and Technology, 77 (2016) 604–609. https://doi.org/10.1007/s10971-015-3889-8
38. Wang, C.-C., Lu, C.-L., Shieu, F.-S., & Shih, H. C. Structure and Photoluminescence Properties of Thermally Synthesized V_2O_5 and Al-Doped V_2O_5 Nanostructures. Materials, 14(2) (2021) 359. https://doi.org/10.3390/ma14020359
39. Lee, J., Lee, D. W., Jeong, H., Park, J., Park, S., Kim, J., Kim, J.-Y., & Lim, S. H. Influence of Nd doping on the structural and electrochemical properties of uranium dioxide. Journal of Nuclear Materials, 593 (2024) 154976. https://doi.org/10.1016/j.jnucmat.2024.154976
40. Le, T. K., Kang, M., Han, S.-W., & Kim, S.-W. Highly intense room-temperature photoluminescence in V_2O_5 nanospheres. RSC Advances, 8(72) (2018) 15334–15341. https://doi.org/10.1039/c8ra06861e
41. Navyashree, G., Hareesh, K., Sunitha, D. V., Nagabhushana, H., & Nagaraju, G. Photocatalytic degradation performance of Nd^{3+} doped V_2O_5 nanostructures. Materials Research Express, 5(2) (2018) 025021. https://doi.org/10.1088/2053-1591/aad373